PERGAMON

International Journal of Heat and Mass Transfer 45 (2002) 775–784

International Journal of HEAT and MASS TRANSFER

www.elsevier.com/locate/ijhmt

Numerical investigation of the three-dimensional natural convection inside horizontal concentric annulus with specified wall temperature or heat flux

Chun-Lang Yeh *

Department of Aeronautical Engineering, National Huwei Institute of Technology, Huwei, Yunlin 632, Taiwan, ROC

Received 5 March 2001; received in revised form 1 June 2001

Abstract

A numerical investigation for three-dimensional natural convection inside horizontal concentric annulus with open ends and conditions of either adiabatic or isothermal outer cylinder surface is made by a zonal grid approach, which extends the outlet boundary from the open end of the annuli to a far enough outside position that can be reasonably specified with the ambient flow properties. Computational result reveals that the maximum inner cylinder surface temperature occurs right at the top of the inner cylinder. It is also found that the inner cylinder surface temperatures decrease towards the outlet plane for the adiabatic case, while remains relatively constant for the isothermal case. The variation of the inner cylinder surface temperatures is smaller for the isothermal case as compared to the adiabatic case.

Keywords: Natural convection; Horizontal concentric annulus; Zonal grid method; Specified wall temperature or heat flux

1. Introduction

Natural convection inside horizontal annulus with open ends occurs in many engineering applications. A typical example is the underground power cable. Heat is generated from the electrical resistance of the power cable and the heat dissipation process in the annulus relies on the natural convection heat transfer from both open ends of the conduit, which penetrate onto the manhole surfaces. The heat dissipation rate is determined from the ventilation stemmed from natural convection and will affect the lifetime of the power cable.

Owing to the symmetric nature of the flow field with respect to the two open ends and to a vertical plane crossing the center of the cylinders, the computational domain is schematically shown in Fig. 1. In addition to the convection heat transfer, a more comprehensive thermal model for the configuration investigated should include the thermal radiation inside the enclosure. However, the present study is focused on the convection problem only. The additional complication due to considerations of thermal radiation in the enclosure is reserved for future study.

The boundary conditions for this problem are as follows. Either adiabatic or isothermal condition is given on the outer cylinder surface, while on the inner cylinder a constant heat flux is given. For the isothermal condition, the outer cylinder surface is maintained at T_{ref} (i.e., 300 K). No slip condition is given to all the three components of the velocity on the outer and inner cylinder surfaces. Since no flow crosses the circumferentially (or longitudinally) symmetric plane, the angular (or axial) velocity vanishes on that plane. The angular (or axial) derivatives of the remaining velocity components and temperature also vanish on the circumferentially (or longitudinally) symmetric plane. Unlike the vertical configuration of eccentric annuli in which the fully developed thermal boundary conditions may be achievable [1], the boundary conditions at the open end of the present problem are much more troublesome. Although this plane is named as the outlet (see Fig. 1) in consideration of the heat dissipation route in the

* Tel.: +886-5-6329643 ext. 363 ext. 36; fax: +886-5-6312415.
E-mail address: clyeh@sunws.nhit.edu.tw (C.-L. Yeh).

0017-9310/02/$ - see front matter
PII: S0017-9310(01)00191-0

Nomenclature

C_p	specific heat capacity
D_h	hydraulic diameter
Ec	Eckert number, $V^{*2}/(C^*_{p_{ref}} q^*_w D^*_h/k^*_{ref})$
Fr	Froude number, $V^*/\sqrt{g^* D^*_h}$
g	gravitational acceleration
g^{jk}	contravariant metric tensor
h	convective heat transfer coefficient
J	Jacobian
k	thermal conductivity
Pr	Prandtl number, υ^*/α^*
p	hydraulic pressure, $(p^* + \rho^*_{ref} g^* y^*)/\rho^*_{ref} V^{*2}$
q	heat flux
q^j	curvilinear coordinate
R^Φ	source term
Ra	Rayleigh number, $g^*\beta^* D^{*3}_h \Delta T^*/\upsilon^*\alpha^*$
Ra^o	modified Rayleigh number, $g^*\beta^* D^{*4}_h q^*_w/\upsilon^*\alpha^* k^*$
T	temperature
(u, v, w)	physical velocity, $(u^*, v^*, w^*)/V^*$
V^j	contravariant velocity
V^*	characteristic velocity, α^*/D^*_h
(x, y, z)	Cartesian coordinates, $(x^*, y^*, z^*)/D^*_h$

Greek symbols

α	thermal diffusivity
β	thermal expansion coefficient
Γ^Φ	diffusion coefficient
θ	non-dimensionalized temperature, $(T^* - T^*_{ref})/(q^*_w D^*_h/k^*)$
μ	viscosity
υ	kinematic viscosity
ρ	density, ρ^*/ρ^*_{ref}
Φ	energy dissipation term; also dependent variable
ϕ	azimuthal angle

Subscripts

i	inner cylinder
nb	neighboring grid points
o	outer cylinder
P	main grid point
ref	reference state (at atmospheric pressure and room temperature)
w	wall

Superscripts

–	averaged quantity
*	dimensional quantity

conduit, it consists of inflow (fresh flowing fluid) and outflow (heated flowing fluid) at the same plane (see Fig. 4). An approach used in the simulations of the non-cavity type, buoyancy-induced flows is the "zonal grid" approach [2,3] which extends the computational domain outside the outlet plane so that the boundary conditions can be reasonably specified with the ambient flow properties. Typical examples can be found in [4,5]. Although this approach requires enormous computations for three-dimensional problems, it provides more reliable results among existing approaches. In this work, the zonal grid approach is adopted to resolve the problem of the outlet boundary conditions.

Many theoretical and experimental studies on natural convection in horizontal concentric annuli have been carried out. In most of these studies, a two-dimensional model was used in which the annuli are assumed to be infinitely long and coupled with thermal boundary conditions on the cylinder surfaces specified, as either with two constant wall temperatures or one with constant wall temperature while the other with constant wall heat flux (including adiabatic surface) [6–14]. However, the boundary conditions on the cylinder surfaces do not permit the solution of a two-dimensional natural convection within the transverse plane in the present work. Three-dimensional formulation has to be used to model the problem. There have been few three-dimensional investigations of natural convection in concentric annuli between two horizontal cylinders, except with the configuration of cavity type [15,16]. A comprehensive literature survey has revealed that published work is largely non-existent on three-dimensional concentric annuli between two horizontal cylinders, where their geometric configurations possess open ends (not annular cavity). The scope of this work is to investigate numerically the flow and thermal fields of laminar natural convection in the geometric configuration schematically shown in Fig. 1.

Since the thermal boundary conditions at the inner cylinder surfaces are specified in terms of heat fluxes instead of temperatures in the present work, a modified Rayleigh number is defined as follows:

$$Ra^o = \frac{g^*\beta^*_{ref} D^{*3}_h}{\upsilon^*_{ref}\alpha^*_{ref}}(q^*_w D^*_h/k^*_{ref}). \quad (1)$$

As pointed out by Kuehn and Goldstein [11], an onset of transition from laminar to turbulent regimes starts near $Ra = 4 \times 10^6$ for gases in a concentric annulus of $D_o/D_i = 2.6$. Moreover, a study by Labonia and Guj [13] indicated that chaotic flows were observed in the range of $0.9 \times 10^5 \leqslant Ra \leqslant 3.37 \times 10^5$ for a concentric annulus of $D_o/D_i = 2.36$. However, their conclusions were drawn from the experimental observations and based upon the cases associated with the constant temperature differences between the outer and inner cylinders. Kumar [9] made a numerical investigation using a

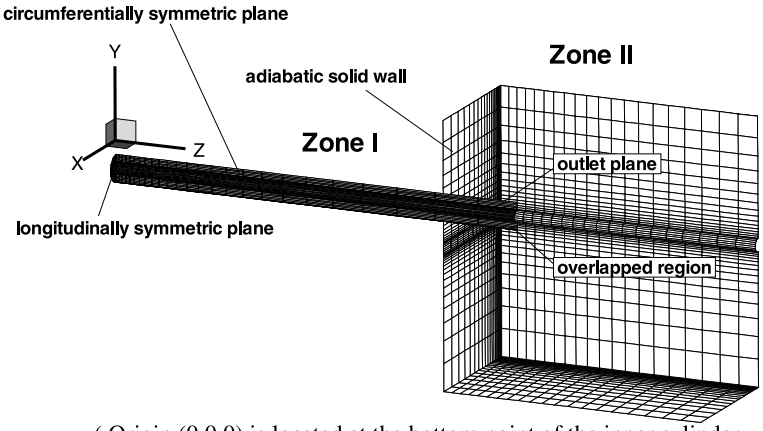

(Origin (0,0,0) is located at the bottom point of the inner cylinder
(a) on the longitudinally symmetric plane, cf. Fig.3)

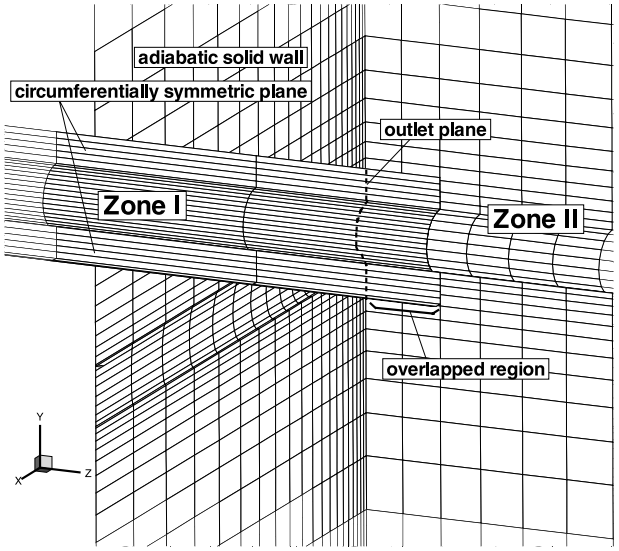

(b)

Fig. 1. Illustration of the computational domain and zonal grid distribution: (a) overall view; (b) zoom-in view near the interface of the two zones.

two-dimensional model for an infinitely long, horizontal, concentric annulus where the inner cylinder was specified by a constant heat flux and the outer cylinder was isothermally cooled. He found that the critical Ra^o above which the numerical results failed to converge were 3.1×10^5 and 3×10^6 at $D_o/D_i = 1.5$ and 2.6, respectively. Kumar also recognized that it was hard to judge whether the flow would become oscillatory or three-dimensional beyond the critical Ra^o for a given ratio of D_o/D_i. The present work, which is essentially a three-dimensional problem with the medium of air ($Pr = 0.7$), encounters the same convergence difficulty beyond $Ra^o = O(10^7)$, which may imply an onset of transition from steady laminar to chaotic or even turbulent flows. Here, the case of $Ra^o = 10^6$, which may lead to distinct temperature variations on the inner cylinder surface, is calculated for demonstration.

2. Mathematical model

The flow pattern of interest here necessitates the solution of three-dimensional fully elliptic type of partial differential equations, which describe the natural convection flow field. Considering the steady-state flow situation, the governing equations in Cartesian coordinates read:

$$\frac{\partial}{\partial x}(\rho u) + \frac{\partial}{\partial y}(\rho v) + \frac{\partial}{\partial z}(\rho w) = 0, \tag{2}$$

$$\frac{\partial}{\partial x}(\rho uu)+\frac{\partial}{\partial y}(\rho vu)+\frac{\partial}{\partial z}(\rho wu) = -\frac{\partial p}{\partial x}+Pr\left[\frac{\partial^2 u}{\partial x^2}+\frac{\partial^2 u}{\partial y^2}+\frac{\partial^2 u}{\partial z^2}+\frac{1}{3}\frac{\partial}{\partial x}\left(\frac{\partial u}{\partial x}+\frac{\partial v}{\partial y}+\frac{\partial w}{\partial z}\right)\right], \tag{3}$$

$$\frac{\partial}{\partial x}(\rho uv)+\frac{\partial}{\partial y}(\rho vv)+\frac{\partial}{\partial z}(\rho wv) = -\frac{\partial p}{\partial y}+Pr\left[\frac{\partial^2 v}{\partial x^2}+\frac{\partial^2 v}{\partial y^2}+\frac{\partial^2 v}{\partial z^2}+\frac{1}{3}\frac{\partial}{\partial y}\left(\frac{\partial u}{\partial x}+\frac{\partial v}{\partial y}+\frac{\partial w}{\partial z}\right)\right]+\frac{1-\rho}{Fr^2}, \tag{4}$$

$$\frac{\partial}{\partial x}(\rho uw)+\frac{\partial}{\partial y}(\rho vw)+\frac{\partial}{\partial z}(\rho ww) = -\frac{\partial p}{\partial z}+Pr\left[\frac{\partial^2 w}{\partial x^2}+\frac{\partial^2 w}{\partial y^2}+\frac{\partial^2 w}{\partial z^2}+\frac{1}{3}\frac{\partial}{\partial z}\left(\frac{\partial u}{\partial x}+\frac{\partial v}{\partial y}+\frac{\partial w}{\partial z}\right)\right], \tag{5}$$

$$\frac{\partial}{\partial x}(\rho u\theta)+\frac{\partial}{\partial y}(\rho v\theta)+\frac{\partial}{\partial z}(\rho w\theta) = \frac{\partial^2\theta}{\partial x^2}+\frac{\partial^2\theta}{\partial y^2}+\frac{\partial^2\theta}{\partial z^2}+Ec\left(u\frac{\partial p}{\partial x}+v\frac{\partial p}{\partial y}+w\frac{\partial p}{\partial z}\right)+Pr\,Ec\,\Phi-\Pi, \tag{6}$$

where

$$\Phi = 2\left[\left(\frac{\partial u}{\partial x}\right)^2+\left(\frac{\partial v}{\partial y}\right)^2+\left(\frac{\partial w}{\partial z}\right)^2\right]+\left(\frac{\partial u}{\partial y}+\frac{\partial v}{\partial x}\right)^2+\left(\frac{\partial u}{\partial z}+\frac{\partial w}{\partial x}\right)^2+\left(\frac{\partial v}{\partial z}+\frac{\partial w}{\partial y}\right)^2-\frac{2}{3}\left(\frac{\partial u}{\partial x}+\frac{\partial v}{\partial y}+\frac{\partial w}{\partial z}\right)^2 \tag{7}$$

and

$$\Pi = \mu^* V^* g^*/q_w^*. \tag{8}$$

Note that the Boussinesq approximation usually made in the formulation of the natural convection is not adopted here and the density is determined using the ideal gas law. The reason of using the ideal gas law rather than Boussinesq approximation for density determination is that the Boussinesq approximation is not valid in case of high temperature difference, which may arise when the Rayleigh number exceeds a critical value. Nevertheless, the maximum temperature rise in the present study is only 15 K (as can be observed from Fig. 6 for the adiabatic case) and therefore the Boussinesq approximation can be used as well.

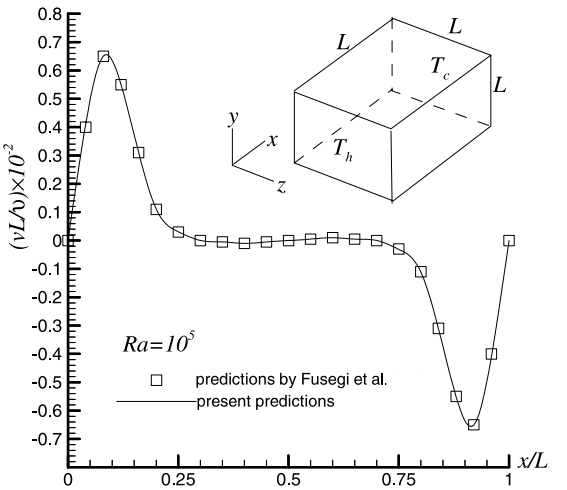

Fig. 2. Velocity vector profile at the middle height in the symmetric plane ($y/L = 0.5$ and $z/L = 0.5$).

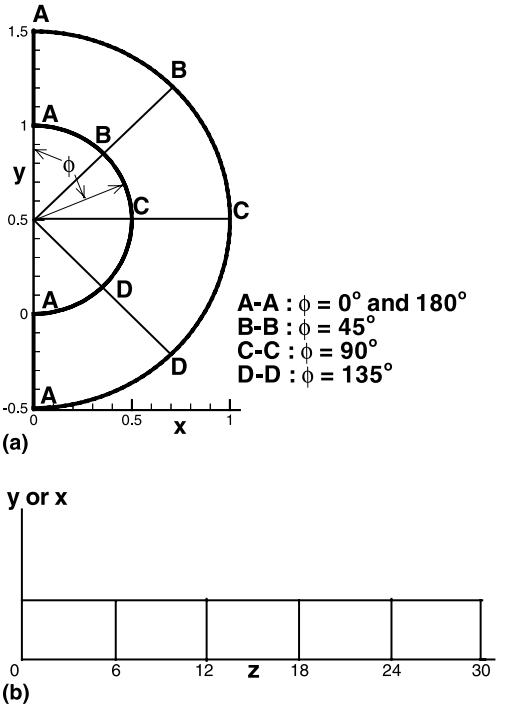

Fig. 3. Illustration of the selected: (a) transverse sections; (b) longitudinal sections.

3. Numerical method

The above governing equations can be cast into the following general form, which permits a single algorithm to be used.

$$\frac{\partial}{\partial x_j}(\rho v_j\Phi) = \frac{\partial}{\partial x_j}\left(\Gamma^\Phi\frac{\partial\Phi}{\partial x_j}\right)+R^\Phi. \tag{9}$$

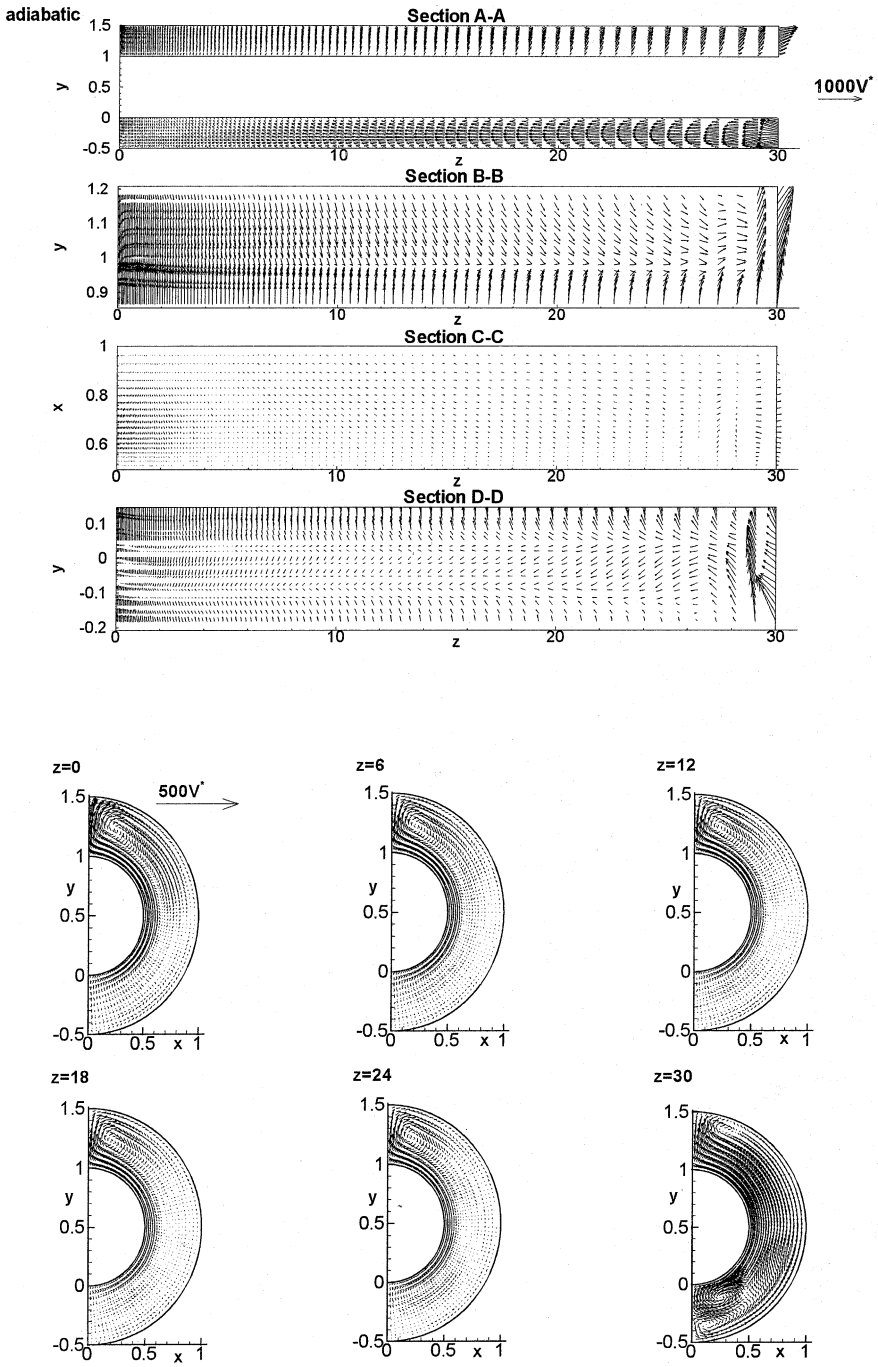

Fig. 4. Velocity vector plots at selected transverse and longitudinal sections.

To facilitate the handling of complex geometry of the present problem, the body-fitted coordinate system is used to transform the physical domain into a computational domain, which is in a rectangular coordinate system with uniform control volumes. Transformation of Eq. (9) to the body-fitted coordinates leads to

$$\frac{\partial}{\partial q^j}(J\rho V^j \Phi) = \frac{\partial}{\partial q^j}\left(Jg^{jk}\Gamma^{\Phi}\frac{\partial \Phi}{\partial q^k}\right) + JR^{\Phi}, \tag{10}$$

where q^j are the curvilinear coordinates (ξ, η, ζ), the Jacobian

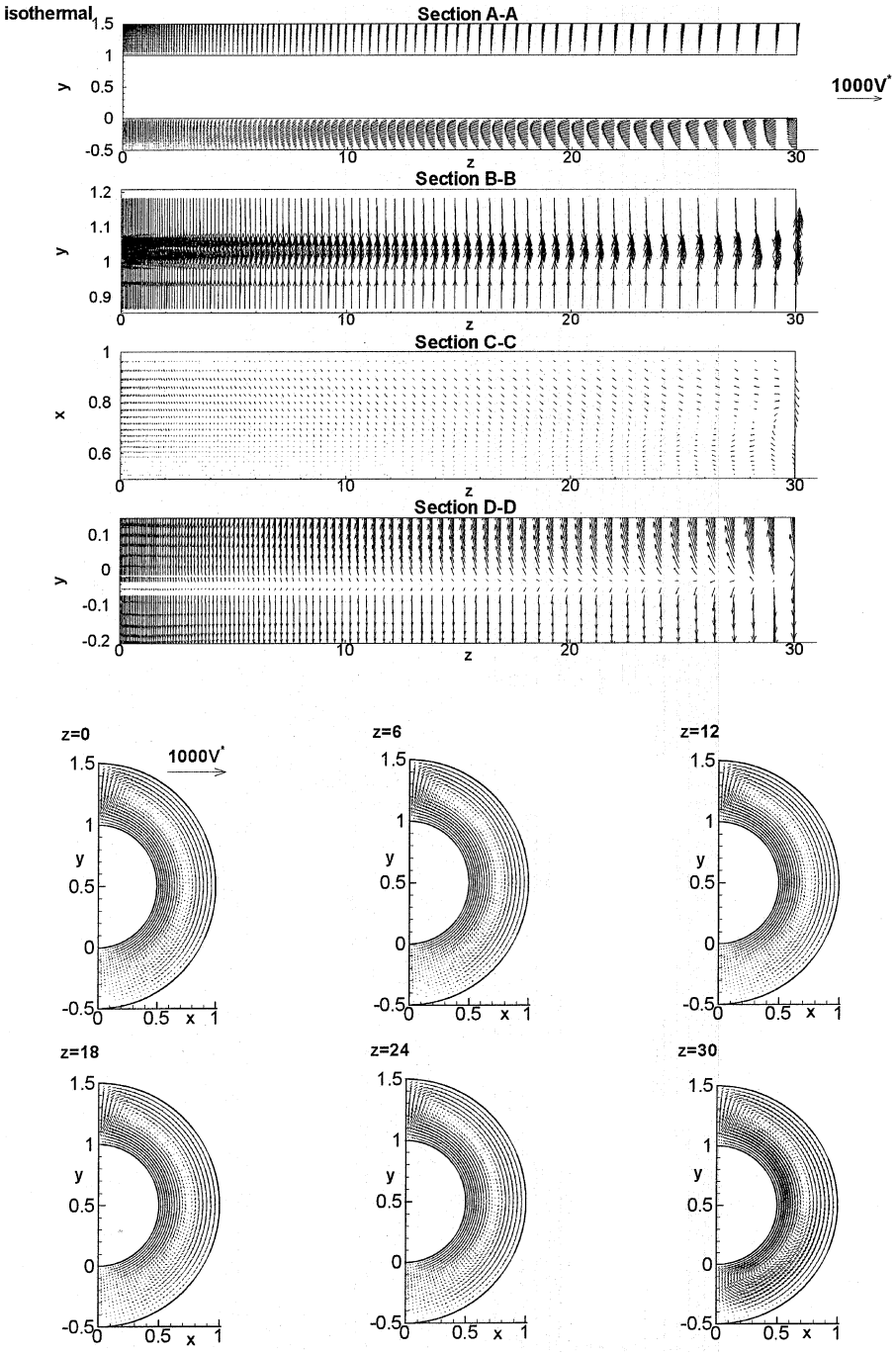

Fig. 4 *(continued)*.

$$J \equiv x_\xi y_\eta z_\zeta + x_\eta y_\zeta z_\xi + x_\zeta y_\xi z_\eta - x_\zeta y_\eta z_\xi - x_\xi y_\zeta z_\eta - x_\eta y_\xi z_\zeta,$$

V^j is the contravariant velocity (U, V, W)

$$U = \frac{1}{J}\left[u(y_\eta z_\zeta - y_\zeta z_\eta) + v(x_\zeta z_\eta - x_\eta z_\zeta) + w(x_\eta y_\zeta - x_\zeta y_\eta)\right],$$

$$V = \frac{1}{J}\left[u(y_\zeta z_\xi - y_\xi z_\zeta) + v(x_\xi z_\zeta - x_\zeta z_\xi) + w(x_\zeta y_\xi - x_\xi y_\zeta)\right],$$

$$W = \frac{1}{J}\left[u(y_\xi z_\eta - y_\eta z_\xi) + v(x_\eta z_\xi - x_\xi z_\eta) + w(x_\xi y_\eta - x_\eta y_\xi)\right],$$

g^{jk} is the metric tensor

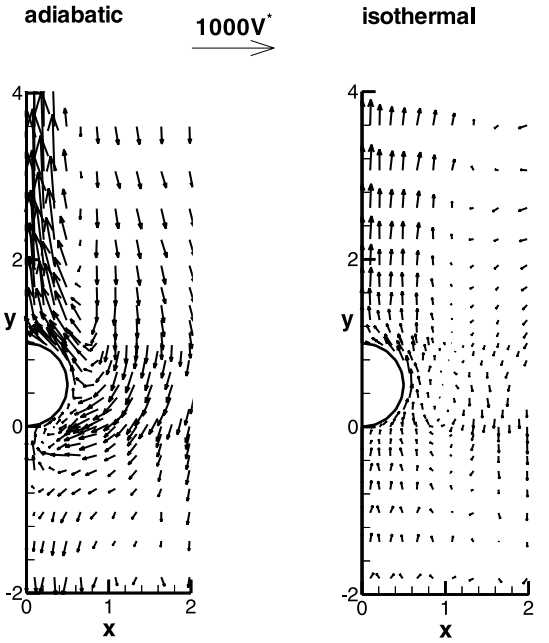

Fig. 5. Velocity vector plots near the end of the annulus ($z = 30.6$).

$$g^{11} = \frac{1}{J^2}\left[(y_\eta z_\zeta - y_\zeta z_\eta)^2 + (x_\zeta z_\eta - x_\eta z_\zeta)^2 + (x_\eta z_\zeta - x_\zeta z_\eta)^2\right],$$

$$g^{12} = g^{21} = \frac{1}{J^2}\left[(y_\eta z_\zeta - y_\zeta z_\eta)(y_\zeta z_\xi - y_\xi z_\zeta) + (x_\zeta z_\eta - x_\eta z_\zeta)(x_\xi z_\zeta - x_\zeta z_\xi) + (x_\eta y_\zeta - x_\zeta y_\eta)(x_\zeta y_\xi - x_\xi y_\zeta)\right],$$

$$g^{13} = g^{31} = \frac{1}{J^2}\left[(y_\eta z_\zeta - y_\zeta z_\eta)(y_\xi z_\eta - y_\eta z_\xi) + (x_\zeta z_\eta - x_\eta z_\zeta)(x_\eta z_\xi - x_\xi z_\eta) + (x_\eta y_\zeta - x_\zeta y_\eta)(x_\xi y_\eta - x_\eta y_\xi)\right],$$

$$g^{22} = \frac{1}{J^2}\left[(y_\zeta z_\xi - y_\xi z_\zeta)^2 + (x_\xi z_\zeta - x_\zeta z_\xi)^2 + (x_\zeta y_\xi - x_\xi y_\zeta)^2\right],$$

$$g^{23} = g^{32} = \frac{1}{J^2}\left[(y_\zeta z_\xi - y_\xi z_\zeta)(y_\xi z_\eta - y_\eta z_\xi) + (x_\xi z_\zeta - x_\zeta z_\xi)(x_\eta z_\xi - x_\xi z_\eta) + (x_\zeta y_\xi - x_\xi y_\zeta)(x_\xi y_\eta - x_\eta y_\xi)\right],$$

$$g^{33} = \frac{1}{J^2}\left[(y_\xi z_\eta - y_\eta z_\xi)^2 + (x_\eta z_\xi - x_\xi z_\eta)^2 + (x_\xi y_\eta - x_\eta y_\xi)^2\right].$$

The grid layout is constructed by connecting the grid points in each transverse plane, which are generated by solving the two-dimensional elliptic type of partial differential equations governing the distribution of the grid points [17]. Numerical calculation of Eq. (10) is performed using the control-volume based finite difference procedure. The discretized governing equations are solved on a non-staggered grid system in association with the SIMPLEC algorithm [18] and QUICK scheme [19].

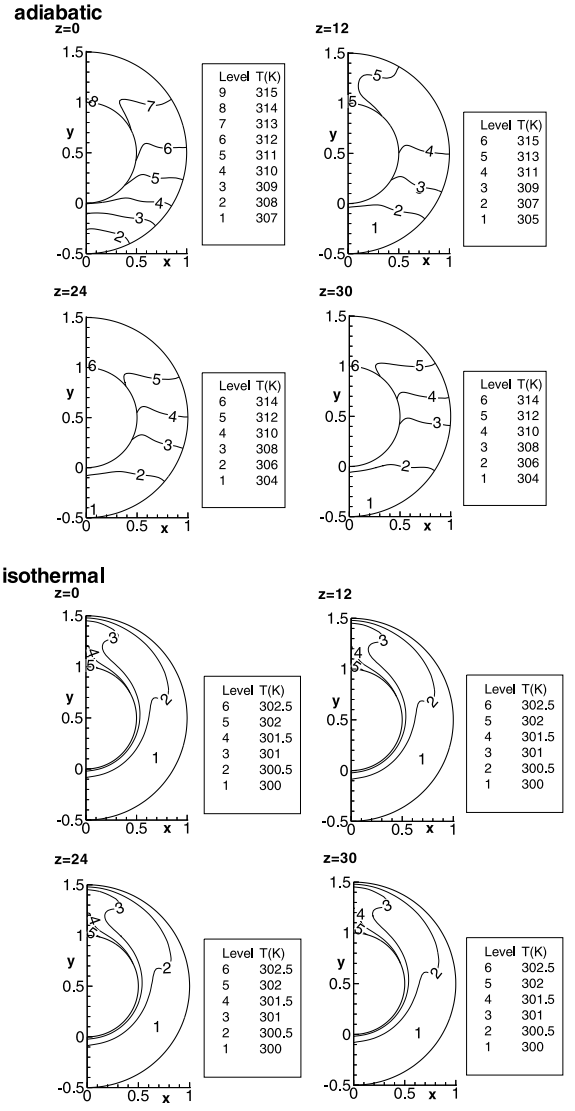

Fig. 6. Temperature contours at selected longitudinal sections.

In the use of the zonal grid approach [4,5], the computational domain is extended outside the outlet plane and is divided into two sub-domains of zones I and II, as schematically illustrated in Fig. 1. The inner and outer diameters of zone I are 0.1 and 0.2 m, respectively, and its length is 3 m (equivalent to $30D_h^*$'s). Computation of a further longer annulus is not permitted due to the limi-

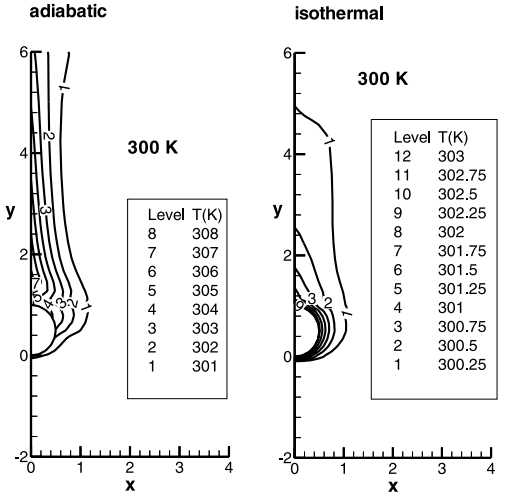

Fig. 7. Temperature contours near the end of the annulus ($z = 30.6$).

tation of the available computational facility. Zone II is constructed by a cube with side length of $20D_h^*$'s to assure its boundary conditions being reasonably specified by the ambient properties. The outer cylinder is flush with the adiabatic solid wall while the inner cylinder extends to the free boundary. The boundary conditions for zone I have been stated in Section 1 and will not be repeated here. The boundary conditions of zone II are as follows. On the surface of the inner cylinder, the same boundary conditions as specified for zone I are used. On the adiabatic solid wall, the no-slip condition and adiabatic wall are specified. The condition of zero normal gradients is met on the symmetric plane except for the normal velocity component, which vanishes naturally. On the free boundaries, the normal gradients of all the dependent variables except for the temperature are set to be zero. The temperature conditions at the free boundaries are specified as follows: When the flow at any such boundary is leaving the domain, the normal temperature gradient is taken as zero. However, when the flow comes into the domain, its temperature is assigned to that of the ambient.

The treatment of the interface of the two zones follows the overlapping grid method [2]. Starting with guessed values, solutions in zone I together with the overlapped region are updated by one sweep of iteration. The updated solutions at the outlet plane of zone I are then interpolated by bilinear interpolation as the boundary conditions of zone II. The solutions in zone II are then updated by one sweep of iteration and are used, in turn, to interpolate the values in the overlapped region, which provide the new boundary conditions for the resolutions of zone I together with the overlapped region. This completes a full solution cycle. In each solution cycle, continuity of the dependent variables and conservation of fluxes are preserved across the interface. In fact, this is the key to the success of the approach. The solution cycle is repeated until the convergence criterion is satisfied. The convergence criterion is described below.

The general form of the discretized governing equations can be written as

$$A_P \Phi_P = \sum_{nb} A_{nb} \Phi_{nb} + b^{\Phi}. \tag{11}$$

Define

$$B_i^{\Phi} = \left| A_P \Phi_P - \sum_{nb} A_{nb} \Phi_{nb} - b^{\Phi} \right|, \tag{12}$$

$$H_i^{\Phi} = |A_P \Phi_P| + \left| \sum_{nb} A_{nb} \Phi_{nb} + b^{\Phi} \right|, \tag{13}$$

$$\lambda^{\Phi} = \frac{\max\left(B_i^{\Phi}\right)}{(1/N)\sum_i H_i^{\Phi}}, \tag{14}$$

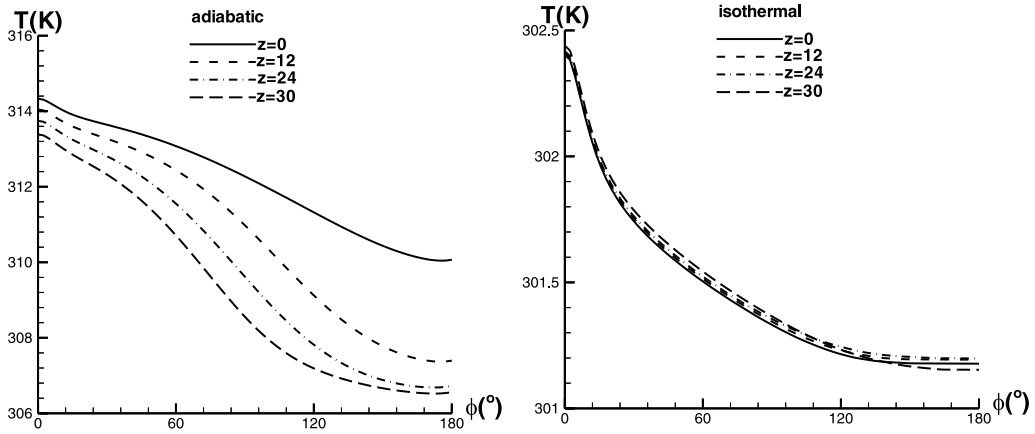

Fig. 8. Azimuthal distributions of the inner cylinder surface temperatures at four longitudinal sections.

where i is an arbitrary grid point in the computational domain and N is the total number of grid points. When $\lambda^{\Phi} \leqslant 1.0 \times 10^{-4}$ for each dependent variable Φ in both the two zones, the iteration process is convergent.

Illustration of the zonal grid distribution is schematically shown in Fig. 1. Numerical tests revealed that the maximum difference in mass inflow rate at the outlet plane between $51 \times 51 \times 101$ (radial $\times$ angular $\times$ axial) and $61 \times 61 \times 121$ grid meshes for zone I, while the corresponding grid meshes for zone II are $21 \times 41 \times 21$ ($x \times y \times z$) and $31 \times 61 \times 31$, respectively, is less than 0.5%. Therefore, the former set of grid mesh is adopted in the present work.

4. Results and discussion

To validate the computer model developed in this work, a benchmark problem of the three-dimensional natural convection in a differentially heated cubical enclosure [20], which is schematically shown in Fig. 2, is first calculated for the case of $Ra = 10^5$ with a $51 \times 51 \times 26$ uniformly distributed grid mesh. The calculated result along the symmetric line ($y/L = 0.5$ and $z/L = 0.5$) is presented in Fig. 2 and compared with the result predicted by Fusegi et al. [20]. An excellent agreement between the present calculation and the one obtained by Fusegi et al. supports the validation of the developed computer model.

Fig. 3 illustrates the section positions of the configuration being studied. Both the adiabatic and isothermal conditions for the outer cylinder surface are examined for the conditions of $r_o/r_i = 2$ and $Ra^o = 10^6$ to investigate the natural convection heat dissipation inside the conduit.

Fig. 4 shows the velocity vector plots at selected transverse and longitudinal sections for the examined cases. Note that the results for sections A–A, B–B and D–D are the vertical projections of the flow field and therefore the ordinate is y, while the result for section C–C is the horizontal projection of the flow field and therefore the ordinate is x. The flow patterns for the two cases are rather different. As observed from the velocity vector plots on the longitudinal sections, there appear secondary flows in all the six longitudinal sections for both cases. The secondary flow of the adiabatic case is stronger than that of the isothermal case. Further downstream, the secondary flows evolve into counter-rotating recirculation zones for the adiabatic case. Another interesting phenomenon can be observed from the velocity vector plots on the transverse sections. For both cases, the inflow paths are clearly observed in the portion below the inner cylinder, whereas the outflow paths are in the portion above. Such flow patterns result obviously from the buoyancy effect, which can be observed in thermal plume phenomena. This can also be seen from the velocity vector plots at a distance slightly outside the open end (i.e., in zone II) shown in Fig. 5, in which the entrainment effect caused by the upward motion of the buoyant flows can also be seen.

Fig. 6 displays the temperature contours at four selected longitudinal sections along the annulus in zone I (see Fig. 3 for the section positions), while Fig. 7 shows the temperature contours at a distance slightly outside the open end for the examined cases. It is observed that higher temperature regions around the inner cylinder surface locate in the upper portion. This can also be seen from the azimuthal temperature distributions along the inner cylinder surface shown in Fig. 8. As pointed out in the above discussion of the flow pattern on the transverse sections, the (hot) outflow is observed in the portions above the inner cylinder, whereas the (cold) inflow in the portions below. The temperature contours at a position slightly outside the annulus, as shown in Fig. 7, consistently reflect the above observation.

Fig. 8 shows the azimuthal temperature distributions along the inner cylinder surface at four selected longitudinal sections. It is clearly seen that the highest temperature occurs right at the top of the inner cylinder (i.e., $\phi = 0^0$). Also from the figure it is observed that the inner cylinder surface temperatures decrease towards the outlet plane for the adiabatic case, while remains relatively constant for the isothermal case. In addition, the variation of the surface temperatures is smaller for the isothermal case. The maximum inner cylinder surface temperature of the isothermal case is lower than that of the adiabatic case by about 11 K.

5. Conclusions

Horizontal concentric annulus with open ends and conditions of either adiabatic or isothermal outer cylinder surface are examined with a three-dimensional formulation of natural convection heat transfer and by a zonal grid approach, which extends the outlet boundary from the open end of the conduit to a far enough outside position that can be reasonably specified with the ambient flow properties. It is found that higher temperatures around the inner cylinder occur in the region near its top. The maximum inner cylinder surface temperature occurs right at the top of the inner cylinder. The inner cylinder surface temperatures decrease towards the outlet plane for the adiabatic case, while remains relatively constant for the isothermal case. The variation of the inner cylinder surface temperatures is smaller for the isothermal case, as compared to the adiabatic case.

Acknowledgements

The authors gratefully acknowledge the grant support from the National Science Council, ROC, under

the contract NSC89-2212-E-150-040. The constructive suggestions from Professor K.C. Chang in National Cheng-Kung University, ROC, are also appreciated.

References

[1] M.A.I. El-Shaarawi, E.M.A. Mokheimer, Free convection in vertical eccentric annuli with a uniformly heated boundary, Int. J. Numer. Meth. Heat Fluid Flow 8 (1998) 488–503.
[2] M.M. Rai, Navier–Stokes simulations of rotor-stator interaction using patched and overlaid grids, AIAA Paper 85-1519, 1985.
[3] D. Lee, C.L. Yeh, Computation of reacting flame stabilizer flows using a zonal grid method, Numer. Heat Transfer 24 (1993) 273–285.
[4] K. Vafai, J. Ettefagh, Thermal and fluid flow instabilities in buoyancy-driven flows in open-ended cavities, Int. J. Heat Mass Transfer 33 (1990) 2329–2344.
[5] T.S. Chang, T.F. Lin, On the reversed flow and oscillating wake in an asymmetrically heated channel, Int. J. Numer. Meth. Fluids 10 (1990) 443–459.
[6] C.J. Ho, Y.H. Lin, Natural convection heat transfer of cold water within an eccentric horizontal cylindrical annulus, J. Heat Transfer 110 (1988) 894–900.
[7] J. Prusa, L.S. Yao, Natural convection heat transfer between eccentric horizontal cylinders, J. Heat Transfer 105 (1983) 108–116.
[8] T.H. Kuehn, R.J. Goldstein, Correlating equations for natural convection heat transfer between horizontal circular cylinders, Int. J. Heat Mass Transfer 19 (1976) 1127–1134.
[9] R. Kumar, Study of natural convection in horizontal annuli, Int. J. Heat Mass Transfer 31 (1988) 1137–1148.
[10] S. Guj, G. Iannetta, G. Moretti, Experimental analysis of thermal fields in horizontally eccentric cylindrical annuli, Exp. Fluids 12 (1992) 385–393.
[11] T.H. Kuehn, R.J. Goldstein, An experimental study of natural convection heat transfer in concentric and eccentric horizontal cylindrical annuli, J. Heat Transfer 100 (1978) 635–640.
[12] T.H. Kuehn, R.J. Goldstein, An experimental and theoretical study of natural convection in the annulus between horizontal concentric cylinders, J. Fluid Mech. 74 (1976) 695–719.
[13] G. Labonia, G. Guj, Natural convection in a horizontal concentric cylindrical annulus: oscillatory flow and transition to chaos, J. Fluid Mech. 375 (1998) 179–202.
[14] E.K. Glakpe, C.B. Watkins Jr., J.N. Cannon, Constant heat flux solutions for natural convection between concentric and eccentric horizontal cylinders, Numer. Heat Transfer 10 (1986) 279–295.
[15] S.V. Iyer, K. Vafai, Buoyancy induced flow and heat transfer in a cylindrical annulus with multiple perturbations, Int. J. Heat Mass Transfer 41 (1998) 3025–3035.
[16] S.V. Iyer, K. Vafai, Effects of a geometric perturbation on buoyancy induced flow and heat transfer in a cylindrical annulus, Int. J. Heat Mass Transfer 40 (1997) 2901–2911.
[17] J.F. Thompson, Z.U.A. Warsi, C.W. Mastin, Chapter VI. Elliptic Generation Systems, Numerical Grid Generation, North-Holland, Amsterdam, 1985, pp. 188–271.
[18] J.P. Van Doormaal, G.D. Raithby, Enhancements of the SIMPLE method for predicting incompressible fluid flows, Numer. Heat Transfer 7 (1984) 147–163.
[19] T. Hayase, J.A.C. Humphrey, R. Grief, A consistently formulated QUICK scheme for fast and stable convergence using finite-volume iterative calculation procedures, J. Comput. Phys. 98 (1992) 108–118.
[20] T. Fusegi, J.M. Hyun, K. Kuwahara, B. Farouk, A numerical study of three-dimensional natural convection in a differentially heated cubical enclosure, Int. J. Heat Mass Transfer 34 (1991) 1543–1557.